Journal of Power Sources 239 (2013) 563–571

Contents lists available at SciVerse ScienceDirect

Journal of Power Sources

journal homepage: www.elsevier.com/locate/jpowsour

X-ray diffraction studies of the electrochemical intercalation of bis(trifluoromethanesulfonyl)imide anions into graphite for dual-ion cells

Guido Schmuelling, Tobias Placke, Richard Kloepsch, Olga Fromm, Hinrich-Wilhelm Meyer**, Stefano Passerini, Martin Winter*

University of Muenster, Institute of Physical Chemistry, MEET Battery Research Center, Corrensstr. 46, D-48149 Muenster, Germany

HIGHLIGHTS

- Electrochemical intercalation of bis(trifluoromethanesulfonyl)imide (TFSI) anions into graphite for dual-ion cells.
- *Ex situ* and *in situ* X-ray diffraction of TFSI intercalation into graphite.
- Calculation of the periodic repeat distance, the intercalant guest gallery height and the gallery expansion for various stages.
- Conclusion of the maximum stoichiometry of the TFSI intercalated graphite at different cell conditions.

ARTICLE INFO

Article history:
Received 24 September 2012
Received in revised form
21 February 2013
Accepted 7 March 2013
Available online 26 March 2013

Keywords:
Anion intercalation
Dual-ion cell
In situ XRD
$Pyr_{14}TFSI$
Staging transitions
Gallery height

ABSTRACT

"Dual-graphite" cells use graphite as intercalation host at both electrodes, where the energy storage mechanism is based on the intercalation of lithium ions into the negative and the intercalation of electrolyte anions into the positive electrode. In this contribution, the electrochemical intercalation of bis(trifluoromethanesulfonyl)imide (TFSI) anions from an ionic liquid-based electrolyte ($Pyr_{14}TFSI$) into graphite was studied using *ex situ* and *in situ* X-ray diffraction. We prove that the TFSI intercalated graphite exists in a series of staged phases. As for this electrode material the discharge capacity can be strongly influenced by the cut-off potential and temperature, the stage transitions and compositions of the TFSI intercalated graphite were determined in dependency of different temperatures and cut-off potentials. From the experimental data, the periodic repeat distance of the graphite intercalation compound, the TFSI gallery height and the maximum stoichiometries of $C_n^+TFSI^-$ at these different conditions are calculated and discussed.

© 2013 Elsevier B.V. All rights reserved.

1. Introduction

Graphite is a redox-amphoteric intercalation host and therefore able to yield so-called donor-type and acceptor-type graphite intercalation compounds (GICs) via electrochemical intercalation of cations and anions at different potentials [1,2]. The current predominantly used donor-type GIC redox couple LiC_x/C_x is the major active compound for state-of-the-art negative electrodes in lithium ion batteries [3–6]. The anions capable to form acceptor-type GICs are mainly fluoro-, chloro-, or oxometalates such as PF_6^-, AsF_6^-, BF_4^- [7–9], $AlCl_4^-$, SO_4^- or NO_3^- [10–12]. In addition, also larger carbon-based anions such as trifluoroacetate (CF_3COO^-) [13] and bis(trifluoromethanesulfonyl)imide ($(CF_3SO_2)_2N^-$) [14,15] have been demonstrated to form acceptor-type GICs.

The hexagonal structure of graphitic carbon with ABAB stacking consists of graphene sheets, which means that the intercalated guests can be accommodated in the gaps between the layers. It is well known, that the process of guest species uptake does not occur in every layer simultaneously. During intercalation the intercalant must overcome the cohesive van-der-Waals energy between two adjacent graphene layers; the electrostatic repulsion between different intercalant layers as well as an intralayer attraction between intercalant atoms induces further intercalation within the same layer contrary to further intercalation into another unoccupied layer [16–19]. These effects are proposed to be responsible for the so-called "staging" mechanism.

The different stages of intercalation into graphite are labeled with respect to the number of carbon layers between each

* Corresponding author. Tel.: +49 251 83 36031; fax: +49 251 83 36032.
** Corresponding author. Tel.: +49 251 83 23430; fax: +49 251 83 36032.
E-mail addresses: hwmeyer@uni-muenster.de (H.-W. Meyer), martin.winter@uni-muenster.de (M. Winter).

0378-7753/$ – see front matter © 2013 Elsevier B.V. All rights reserved.
http://dx.doi.org/10.1016/j.jpowsour.2013.03.064

intercalated molecule layer (Fig. 1). Therefore, the maximum stage of intercalation is stage 1, i.e. with only one carbon layer in between two intercalant guest layers. The GICs generally display well-defined stages (n) that can be related to the periodic repeat distance (I_c), the intercalant gallery height (d_i) and the gallery expansion (Δd) by using

$$I_C = d_i + 3.35\ \text{Å}\cdot(n-1) = \Delta d + 3.35\ \text{Å}\cdot n = l\cdot d_{obs} \quad [1]$$

where l is the index of (00l) planes oriented in the stacking direction and d_{obs} is the observed value of the spacing between two adjacent planes [20,21]. Therefore, a well suited technique to observe and determine the staging mechanism of intercalation processes into graphitic carbon is X-ray diffraction.

Recently, we reported that "dual-ion cells" [22,23] based on the intercalation of bis(trifluoromethanesulfonyl)imide (TFSI) anions into a graphite positive electrode from a well suited ionic liquid-based electrolyte with a high stability vs. oxidation, namely *N*-butyl-*N*-methylpyrrolidinium bis(trifluoromethanesulfonyl)imide ($Pyr_{14}TFSI$) [24–30], delivered very promising electrochemical results. These dual-ion cells are superior to existing dual-ion cell systems [31–34] concerning their electrochemical performance in terms of discharge capacity (exceeding 100 mAh g^{-1} based on the graphite cathode weight), cycling stability and coulombic efficiency (99% after 500 cycles) depending on the applied cut-off potential and temperature [22,23].

In this contribution, we investigate the staging mechanism of the bis(trifluoromethanesulfonyl)imide (TFSI) anion intercalation into a graphite positive electrode using *ex situ* and *in situ* X-ray diffraction techniques in combination with cyclic voltammetry and constant current charge/discharge cycling. The dual-ion system investigated in this work is based on a graphite cathode, a metallic lithium anode and an ionic liquid electrolyte containing lithium bis(trifluoromethanesulfonyl)imide (LiTFSI) as electroactive salt in *N*-butyl-*N*-methylpyrrolidinium bis(trifluoromethanesulfonyl) imide ($Pyr_{14}TFSI$), which offers the exceptional stability needed at higher electrode potentials [28].

As the discharge capacity for the dual-ion system can be tailored by either the cut-off potential or the temperature [23] a systematic investigation of the staging transitions and compositions of the staged phases is performed at different cut-off potentials and temperatures, namely at 20 °C and 60 °C. From our results we are able to deduce the periodic repeat distance (I_c) and TFSI gallery heights (d_i) for different stage-*n*-GICs. Moreover, TFSI intercalated structures and stoichiometries, $C_n^+TFSI^-$, providing different stages, are proposed by correlating the X-ray diffraction results and the TFSI dimensions to the obtained discharge capacity and the theoretical specific discharge capacities.

2. Experimental

Electrode films of the positive electrodes consisted of a composition of 90 wt. % of synthetic graphite TIMREX® KS6 (TIMCAL®, d_{50} = 3.2 μm/d_{90} = 6 μm), 5 wt. % of sodium carboxymethylcellulose (CMC) as binder (Walocel CRT 2000 PPA 12, Dow Wollf Cellulosics®) and 5 wt. % of conductive carbon black agent C-nergy Super C65 (TIMCAL®). At first, the binder polymer was allowed to dissolve in de-ionized water to form a 2.5 wt. % solution. Adding the required amount of conductive agent Super C65 to the binder/water mixture was followed by magnetic stirring to obtain a homogenized slurry. Shortly after the addition of KS6 graphite, the slurry was dispersed using a T 25 Ultra Turrax® (1 h, 5000 rpm) to receive a well homogenized, non agglomerated paste. The paste was cast on a freshly etched aluminum foil (30 μm, purity >99.9%, etched with 5 wt. % KOH) applying a standard lab-scale doctor-blade equipment. The gap of the doctor blade was set to 120 μm wet film thickness, leading to an average graphite cathode mass loading of 2.5 mg cm^{-2}. After casting, the tapes were transferred into an atmospheric oven and dried for 12 h at 80 °C. Electrodes with a diameter of 12 mm were cut out and a further drying step was

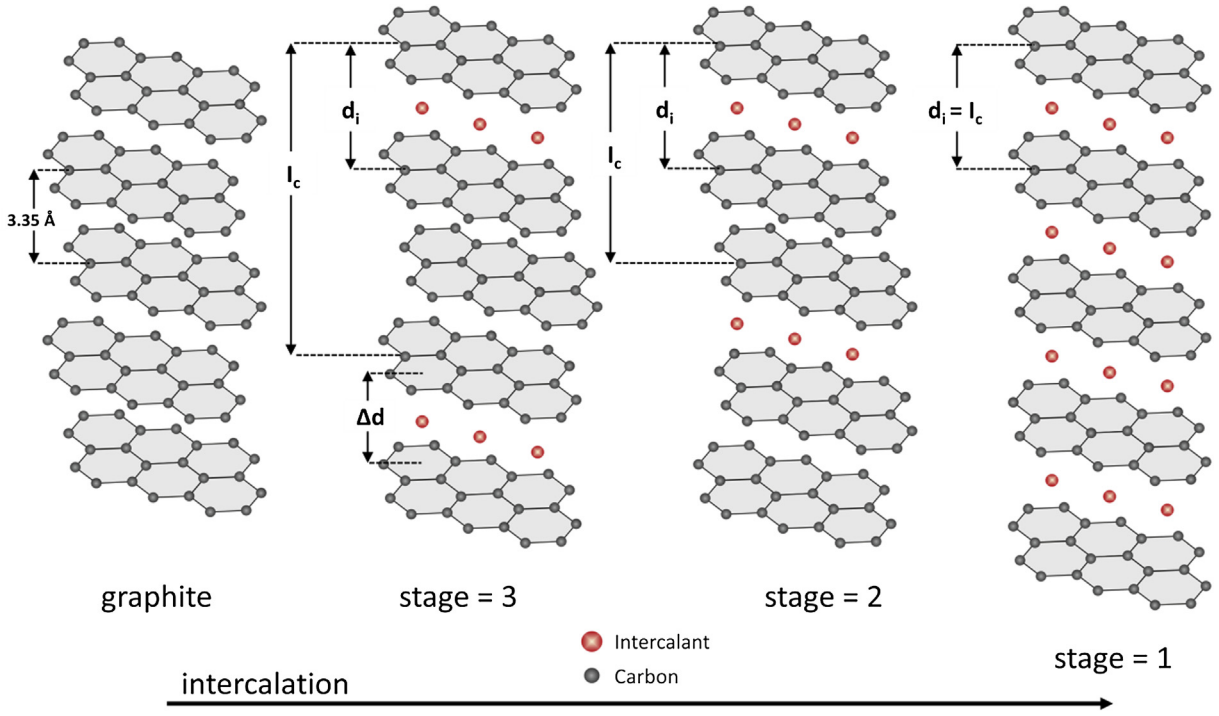

Fig. 1. Schematic illustration of the staging mechanism of intercalant guest species into graphite: I_c = periodic repeat distance; d_i = intercalant gallery height; Δd = gallery expansion. Stage 1 intercalated graphite depicted on the right side being the maximum possible intercalation stage.

performed under a vacuum rotative pump at 170 °C for 24 h. Thereafter, the electrodes were stored in an Argon filled glove box (UniLab, MBraun) with water and oxygen vapor contents below 1 ppm.

Electrochemical investigations were carried out in lab-scale, Swagelok® type, T-cells with three-electrode configuration. In all measurements high-purity metallic lithium foil (Rockwood Lithium®) was used as counter and reference electrode. As a separator, a glass microfiber filter (Whatman®, grade GF/D) was used and as electrolyte *N*-butyl-*N*-methylpyrrolidinium bis(trifluoromethane sulfonyl)imide ($Pyr_{14}TFSI$, Solvionic®, purity: 99.9%) with 1 M of lithium bis(trifluoromethanesulfonyl)imide (LiTFSI, 3 M, purity: 99.95%), not only as conductor (the ionic liquid is conductive as well), but also as electroactive salt (Li^+ and $TFSI^-$ ions are taking part in the charge/discharge mechanism) was applied (molar ratio of $LiTFSI:Pyr_{14}TFSI = 1:3.34$). The received ionic liquid was additionally dried, applying an ultra-high vacuum procedure to obtain water content of less than 10 ppm, determined by Karl Fischer titration.

Charge/discharge cycling was performed on a multichannel Maccor® 4300 battery test system. The charge and discharge steps were performed using a constant current setup, which corresponds to a constant current rate of 50 mA g^{-1} as determined by the weight of the graphite positive electrode. Constant current charge/discharge cycling was performed by charging the cell to an upper cut-off potential ranging from 4.8 to 5.2 V vs. Li/Li^+ (intercalation) while for the de-intercalation/stripping process (discharge) a cut-off potential of 3.4 V vs. Li/Li^+ was chosen. The charge/discharge cycling experiments were performed in climatic chambers at temperatures of 20 °C or 60 °C. For the *ex situ* XRD measurements, the cells were cycled 50 times at different cut-off potentials in the range from 4.8 to 5.2 V vs. Li/Li^+, followed by a constant voltage step at the upper cut-off potential. The cells were then immediately disassembled under dry atmosphere; the graphite cathodes were freed from residual separator and directly placed in the X-ray diffractometer.

In situ XRD data was acquired in a Bragg–Brentano $\theta/2\theta$ geometry requiring an X-ray transparent window, which was implemented in a commercial CR2016 coin cell (Hohsen, Japan). Therefore, a hole with a diameter of 16 mm was punched into a coin cell can ($\varnothing = 20$ mm). To maintain the sealing of the cell system, a circular piece of KAPTON 500HN foil ($\varnothing = 18$ mm, DuPont, 127 μm) was bound to the inner rim of the can using a two-component epoxy resin (TorrSeal®, Varian Inc.), resulting in a window for the transmission of X-rays. An aluminum thin film (not observable in XRD, 100 nm) was sputtered onto the KAPTON foil as current collector using a sputter device (Q150T ES, Quorum Technologies) to provide electronic conductivity to the coin cell can. The graphite paste mentioned above was applied on the sputtered aluminum film to obtain an average mass loading of 3 mg cm^{-2} after drying the coin cell cap at 100 °C for 24 h. After assembly analogous to the Swagelok® type T-cells under dry atmosphere the cells were also directly placed in the X-ray diffractometer.

The X-ray diffraction measurements were carried out using a BRUKER D8 Advance X-ray diffractometer equipped with a copper

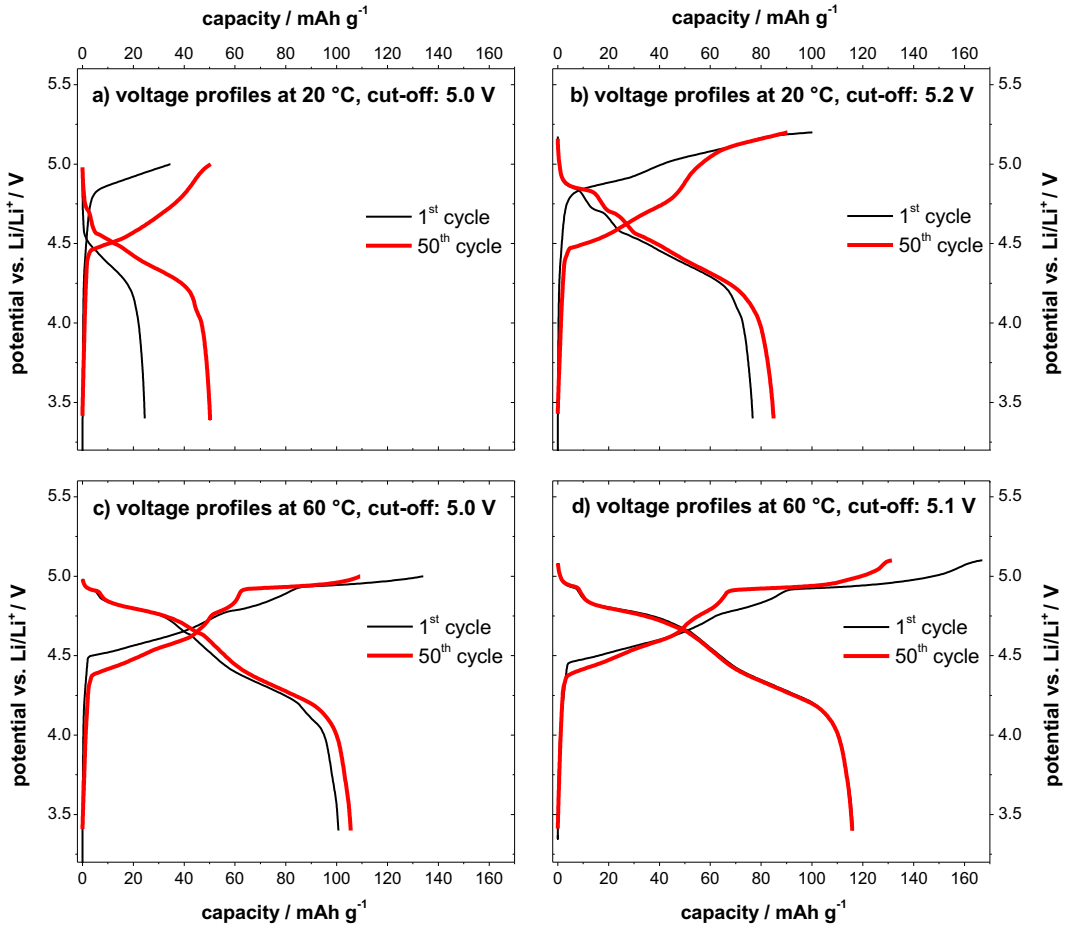

Fig. 2. Potential profiles displaying the 1st and 50th constant current charge/discharge cycle of the metallic lithium/KS6-graphite dual-ion cell with upper cut-off potentials of (a) 5.0 V vs. Li/Li^+ at 20 °C, (b) 5.2 V vs. Li/Li^+ at 20 °C, (c) 5.0 V vs. Li/Li^+ at 60 °C and (d) 5.1 V vs. Li/Li^+ at 60 °C (current rate: 50 mA g^{-1}).

target X-ray tube in a range between $2\theta = 20°$ and 35° with a step size of .0185° per second resulting in 20 min per *in situ* XRD scan at an accelerating voltage of 40 kV and a current flow of 40 mA. Different temperatures, namely, 20 °C and 60 °C, during *in situ* XRD experiments were achieved by embedding the cell into a home-designed XRD sample holder equipped with a heating foil and a resistance thermometer. For *in situ* XRD measurements, cyclic voltammetry was performed using a VSP multichannel constant voltage–constant current system (Biologic® Science Instrument, France) with a scan rate of 50 μV s^{-1} between a cell voltage of 3.4 and 5.2 V for the 20 °C respective 5.1 V for the 60 °C measurements with a 3 h constant voltage step at the upper cut-off voltage.

3. Results and discussion

3.1. Influence of cut-off potential and temperature on the electrochemical intercalation of TFSI anions into KS6-graphite

As we have reported recently, the discharge capacity for the metallic lithium/KS6-graphite dual-ion cell (further abbreviated as Li/KS6) with 1 M LiTFSI–Pyr_{14}TFSI electrolyte is highly dependent on the applied cut-off potential as well as the applied temperature [23,35]. Fig. 2 displays the potential vs. specific capacity profiles for the Li/KS6 dual-ion cell during selected cycles (1st and 50th) of the constant current charge/discharge process at two different temperatures, namely 20 °C and 60 °C, and different cut-off potentials. At a first glance, it is obvious that by increasing the temperature as well as the cut-off potential, increased TFSI anion intercalation and discharge capacity is achieved. Whereas at 20 °C and a cut-off potential of 5.0 V vs. Li/Li^+ a discharge capacity of only 50 mAh g^{-1} was obtained, increasing the cut-off potential to 5.2 V vs. Li/Li^+ resulted in an increase of the discharge capacity to 85 mAh g^{-1}. Increasing the temperature to 60 °C delivers even higher discharge capacities (105 mAh g^{-1} at 5.0 V vs. Li/Li^+ and 115 mAh g^{-1} at 5.1 V vs. Li/Li^+). Furthermore, the potential regions of intercalation and de-intercalation of the TFSI anions are dependent on the applied temperature. An observable trend is that, the higher the applied temperature, the lower the potential where the intercalation in the 1st cycle starts to take place. This effect is proposed to be due to different kinetic hindrances like the widening of the graphite interlayer gaps at the electrode/electrolyte interface [36], the need to overcome the limited wetting at this interface or in the electrode pores [37] and/or the possible graphene layer wrinkling and partial closure of the graphite interlayer gaps due to milling during the manufacturing of the graphite powder [23]. The relatively high salt concentration of the 1 M LiTFSI–Pyr_{14}TFSI electrolyte was proven

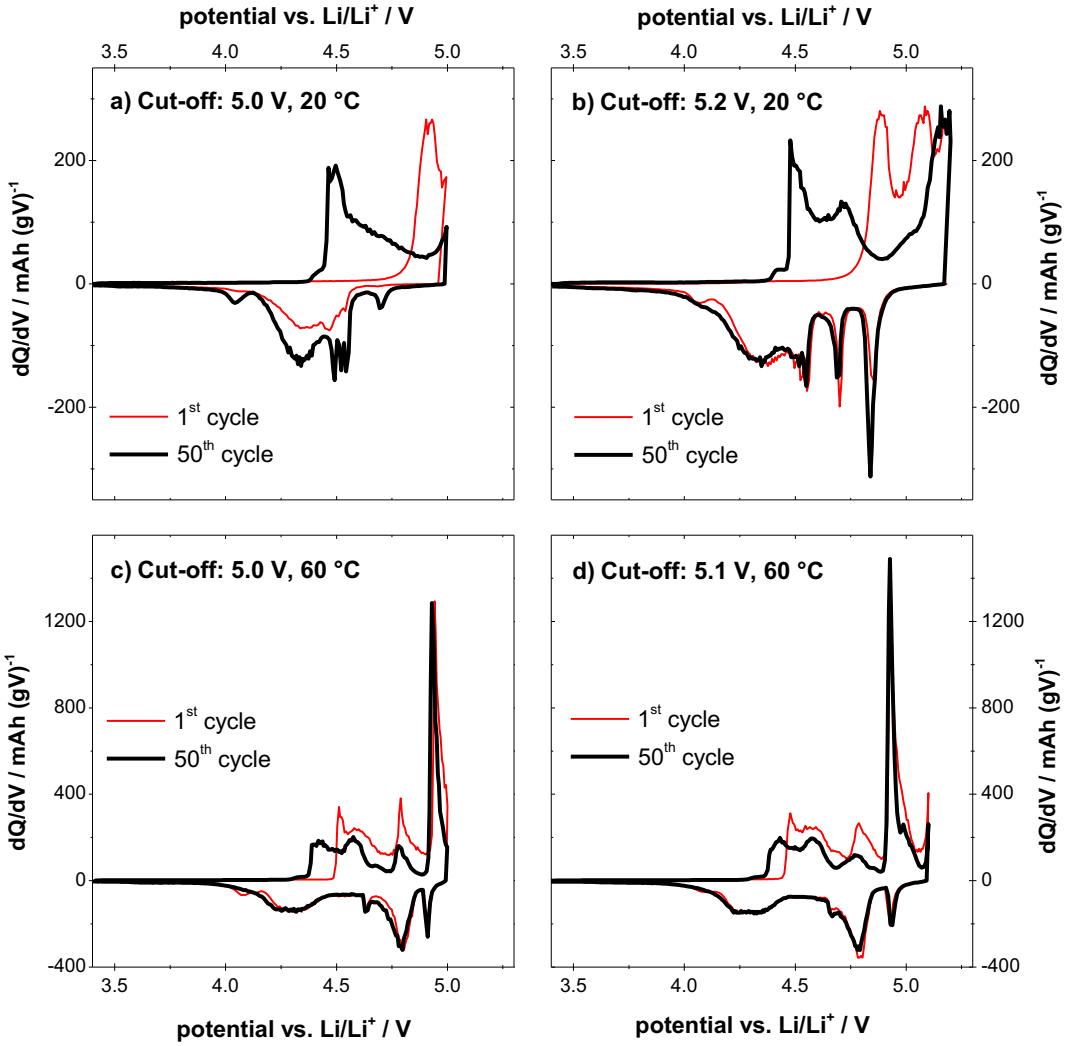

Fig. 3. Differential capacity plots of the metallic lithium/KS6-graphite dual-ion cell during the 1st and 50th cycle of the constant current charge/discharge process at different upper cut-off potentials and temperatures, (a) 5.0 V vs. Li/Li^+ at 20 °C, (b) 5.2 V vs. Li/Li^+ at 20 °C, (c) 5.0 V vs. Li/Li^+ at 60 °C and (d) 5.1 V vs. Li/Li^+ at 60 °C (current rate: 50 mA g^{-1}).

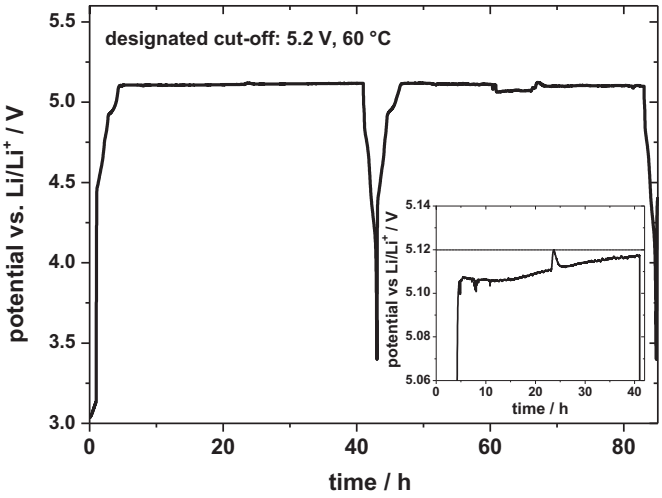

Fig. 4. Potential vs. time profile of the metallic lithium/KS6-graphite dual-ion cell during the constant current charge/discharge process with a designated upper cut-off potential of 5.2 V vs. Li/Li^+ at 60 °C. The charge process is stopped after 40 h, followed by the discharge process.

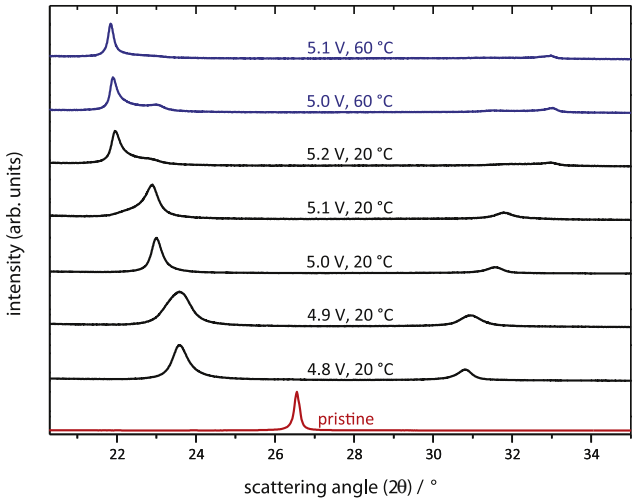

Fig. 6. *Ex situ* X-ray diffraction patterns of KS6-graphite electrodes charged at different temperatures and with cut-off potentials for the metallic lithium/KS6-graphite dual-ion cell (charged: 50 cycles; current rate: 50 mA g^{-1}).

not to have a significant effect, as all shown results in this contribution were also obtained when using .3 M LiTFSI–Pyr_{14}TFSI electrolyte. This kind of "activation" or "formation" during the first anion uptake is followed by a more reversible and reproducible behavior in the ongoing cycles. Therefore, the opening process of the graphite interlayer gaps seems to be limited to the first anion intercalation and will most likely depend on the specific surface area of the graphite particles [38] and in particular on the fraction of prismatic surfaces [39–41], as, like for the lithium ions [42], the anion intercalation can only take place through prismatic-surface sites. It is also clear that at higher temperatures this kinetic effect diminishes. At 60 °C, the anion intercalation begins at a lower potential of about 4.5 V vs. Li/Li^+, compared to 4.8 V vs. Li/Li^+ at 20 °C (Fig. 2a and c). Higher temperatures lead to an easier anion uptake into graphite, which, in turn, results in higher discharge capacities. Besides the above mentioned effects concerning the graphite/electrolyte interface ("opening" and wetting), an additional improvement could derive from the increased ionic conductivity and thus increased mobility of the TFSI anions at elevated temperature [43].

By plotting the cycling curves of the 1st and 50th constant current charge/discharge cycles as differential capacity profiles (Fig. 3), the different potential regions of intercalation and de-intercalation of the TFSI anions are easier to visualize and identify. By comparing the two differential capacity plots at 20 °C (Fig. 3a and b) it is obvious that, instead of one broad peak representing the intercalation stage (in the range of 4.4–5.0 V vs. Li/Li^+) and two peaks corresponding to the de-intercalation stages (at about 4.7 V and from 4.6 to 4.0 V vs. Li/Li^+) at a cut-off potential of 5.0 V vs. Li/Li^+ (Fig. 3a), further intercalation and de-intercalation peaks (at 5.1 and 4.8 V vs. Li/Li^+, respectively) appear by increasing the cut-off potential to 5.2 V vs. Li/Li^+ (Fig. 3b). For the cells with a cut-off potential of 5.0 V vs. Li/Li^+ at 60 °C (Fig. 3c), three main intercalation stages are observable in the potential ranges 4.35–4.65 V, 4.75–4.85 V and 4.9–5.0 V vs. Li/Li^+, with the most dominant one in the highest potential range. Four stages (ca.

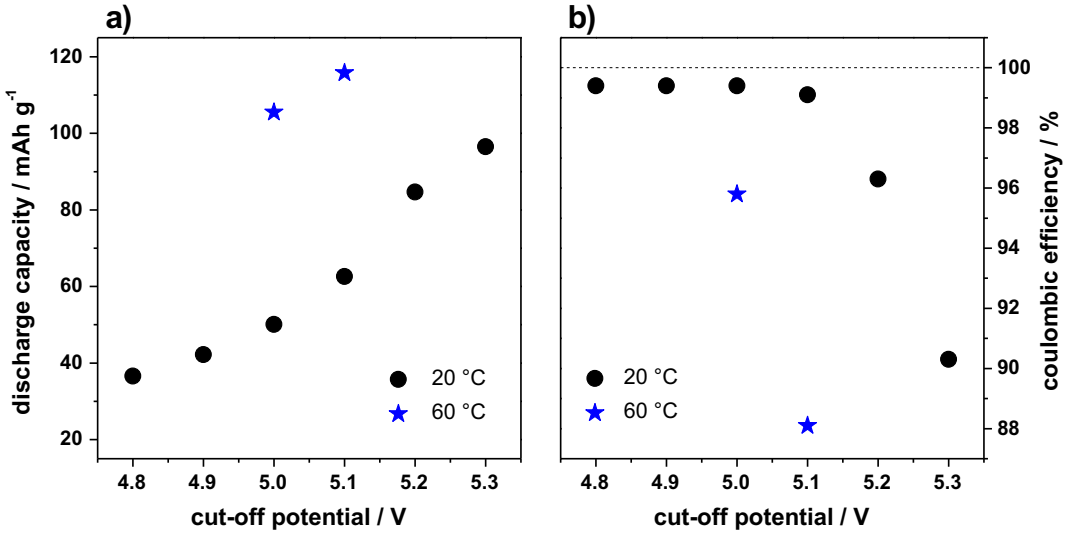

Fig. 5. Correlation of the upper cut-off potential to (a) the discharge capacity and (b) the coulombic efficiency at 20 °C and 60 °C for the metallic lithium/KS6-graphite dual-ion cell (current rate: 50 mA g^{-1}). Data obtained from the 50th charge/discharge cycle of the constant current cycling experiment.

Table 1
The $d_{(n+2)}/d_{(n+1)}$ ratios of a stage n GIC and the most dominant (00l) peak. According to Ref. [44].

Stage, n	$d_{(n+2)}/d_{(n+1)}$ peak position ratio	Dominant (00l) peaks
1	1.50	002
2	1.33	003
3	1.25	004
4	1.20	005
5	1.17	006
6	1.14	007

4.9 V, from 4.85 to 4.7 V, ca. 4.6 V and from 4.5 to 4.0 V vs. Li/Li^+) are visible for the anion de-intercalation process. A very similar peak diagram is depicted for the cell with a cut-off potential of 5.1 V vs. Li/Li^+ at 60 °C (Fig. 3d), except the additional peak shaping up close to the upper cut-off potential, which could be due to electrolyte decomposition. To clarify possible electrolyte decomposition, an experiment with a cell cut-off potential of 5.2 V vs. Li/Li^+ at 60 °C was set up. Fig. 4 clearly displays, that in the region above 5.1 V vs. Li/Li^+ at 60 °C electrolyte decomposition takes place (observable in the long plateau of the potential), which could only be terminated as a time criteria of 40 h was reached. This electrolyte decomposition at 60 °C mainly takes place in the voltage region (potential plateau) from 5.10 to 5.12 V vs. Li/Li^+. Thus for the *in situ* XRD investigations a maximum cut-off potential of 5.10 V vs. Li/Li^+ at 60 °C was chosen.

The correlation of the obtained discharge capacity and coulombic efficiency is depicted in Fig. 5. Although the obtained discharge capacity is increasing with the applied cut-off potential, the coulombic efficiency decreases when exceeding a certain cut-off potential. This effect is probably mainly due to self discharge reaction of the TFSI–graphite intercalation compound at higher temperatures associated to electrolyte decomposition at high potentials, as mentioned before [23,35].

3.2. Ex situ X-ray diffraction investigation

As mentioned above, depending on the applied cut-off potential and temperature of the Li/KS6 dual-ion cell, we were able to obtain different discharge capacities as well as certain regions and plateaus of TFSI intercalation. Therefore, we expected to see varying X-ray diffraction patterns for the various cell setups.

Fig. 6 displays the *ex situ* X-ray diffraction measurements of KS6 graphite cathodes in the Li/KS6 cell cycled at a constant current. For the *ex situ* XRD measurements, the graphite cathodes were charged (intercalated with TFSI anions) at different applied cut-off potentials and temperatures (for details see Experimental section). The scan for the pristine KS6 electrode shows the (002) peak of graphite as expected at $2\theta = 26.55°$. By charging the dual-ion cell to 4.8 V vs. Li/Li^+ at 20 °C with a constant current of 50 mA g^{-1}, the (002) peak has completely vanished and two new peaks at 23.6° and 30.8° have risen. This intensity pattern is a common example for a stage n GIC, where the most dominant peak is the $(00n + 1)$ and the second most dominant peak is the $(00n + 2)$ [14,44]. By determining the ratio of the $d_{(n+2)}/d_{(n+1)}$ peak positions and correlating these to the ratios of stage pure GICs, depicted in Table 1, one is able to assign the most dominant stage phase of the observed GIC [14,44]. Assigning the (00l) indices and using equation (1), one is able to calculate the periodic repeat distance (I_c), the intercalant gallery height (d_i) and the gallery expansion (Δd) [14,44].

The resulting values for the various applied cut-off potentials and temperatures are shown in Table 2. By increasing the cut-off potential from 4.8 to 5.1 V vs. Li/Li^+ at 20 °C the distance between the $(00n + 1)$ and $(00n + 2)$ peak is gradually increasing, as more TFSI is intercalated (increased discharge capacity), although the dominant stage remains stage 2. When applying higher potentials at 20 °C (5.2 V vs. Li/Li^+) or 60 °C, stage 1 TFSI intercalated graphite can be obtained. Whereas at 5.2 V vs. Li/Li^+ and 20 °C as well as at 5.0 V vs. Li/Li^+ and 60 °C a minor shoulder of stage 2 GIC can be identified, at 5.1 V vs. Li/Li^+ and 60 °C only stage 1 intercalated graphite remains. However, the periodic repeat distance within the same stage as well as the TFSI gallery height, namely 8.10 Å ± .01 Å, does not seem to depend on the obtained stage and therefore, not on the obtained TFSI concentration within the graphite. This stage independency of d_i is in agreement with several reported GICs in literature [20]. It is obvious that the ratio of the $d_{(n+2)}/d_{(n+1)}$ peak positions does not always match the theoretical values for the pure stage n GICs. This indicates that, although a dominant stage can be assigned quite easily, the graphene sheets bend, forming intercalate islands with minor different structural regions like interlayer defects or terminating graphene layers. This phenomenon is known as the Daumas–Herold staging model, where there are no completely unfilled layers [45,46].

3.3. In situ X-ray diffraction investigation

In situ XRD investigations were carried out during cyclic voltammetry experiments with a cell voltage in between 3.4 V and 5.2 V at 20 °C or 5.1 V at 60 °C. Figs. 7 and 8 display the first cycle of the *in situ* X-ray diffraction investigations as well as the cyclic voltammetry measurements for 20 °C and 60 °C, respectively. For a better visualization the first 23 XRD scans in the back of Figs. 7 and 8 (at low cell voltages) are not depicted as the (002) peak of graphite with a relatively high intensity remains unaffected until a certain voltage is reached. By drawing an imaginary horizontal line on either side of the XRD patterns, one is able to correlate the regarded XRD scan to the actual applied voltage and current flowing. Table 3 summarizes the values for the dominant stage n, the periodic repeat distance I_c, the TFSI gallery height d_i and the gallery expansion Δd as well as the cell voltage for several scans in the XRD spectra. For both measurements the first observable intercalation stage is 4 starting at scan 26 at about 4.7 V for the 20 °C investigation and at scan 27 at 4.6 V for 60 °C, respectively (rear red lines). TFSI intercalation starting at a slightly lower voltage for the elevated temperature measurement is perfectly reasonable

Table 2
The dominant stage index and calculated values for the *ex situ* X-ray diffraction measurements of TFSI intercalated KS6-graphite electrodes of the lithium/KS6-graphite dual-ion cell at different cut-off potentials and temperatures (data corresponding to Fig. 6).

Temperature/°C	20					60	
Cut-off potential/V	**4.8**	**4.9**	**5.0**	**5.1**	**5.2**	**5.0**	**5.1**
$d_{(n+2)}/d_{(n+1)}$ ratio	1.30	1.31	1.37	1.39	1.50	1.51	1.51
Dominant stage (n)	2	2	2	2	1	1	1
Periodic repeat distance (I_c)/Å	11.45 ± .15	11.43 ± .12	11.46 ± .13	11.44 ± .20	8.12 ± .03	8.12 ± .01	8.14 ± .01
TFSI gallery height (d_i)/Å	8.10	8.08	8.11	8.09	8.12	8.12	8.14
TFSI gallery expansion (Δd)/Å	4.75	4.73	4.76	4.74	4.77	4.77	4.79
Discharge capacity (50th cycle)/mAh g^{-1}	36	42	50	63	85	106	115

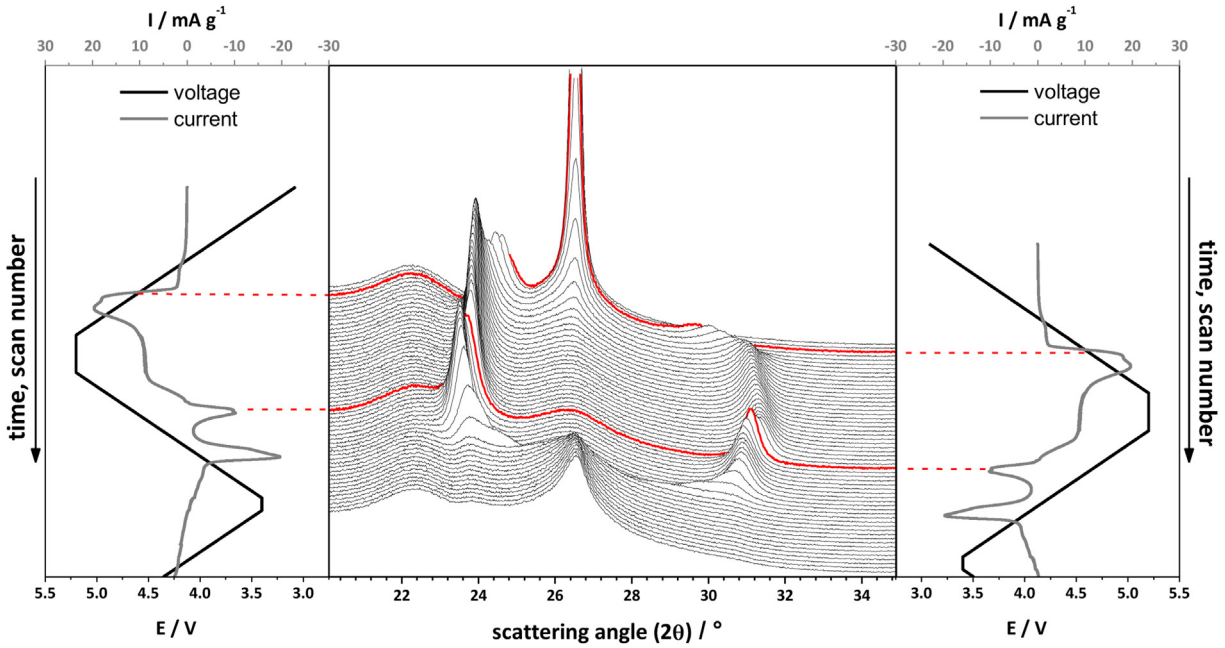

Fig. 7. *In situ* X-ray diffraction patterns as well as cyclic voltammetry profile for the metallic lithium/KS6-graphite dual-ion cell cycled at 20 °C (red lines indicating the beginning of intercalation and deintercalation; scan rate: 50 μV s^{-1}). (For interpretation of the references to colour in this figure legend, the reader is referred to the web version of this article.)

taking into account the electrochemical investigations and the diminishing kinetic hindrance at elevated temperatures as discussed above (see also: Ref. [23]). Passing stage 3 intercalated graphite by scan 29 around 4.8 V at 20 °C the maximum stage of intercalation (2) of the measurement is reached. Even a constant voltage step at 5.2 V for 3 h did not change the stage phase in the first cycle. However, at 60 °C two distinct and one broad intercalation peak, probably representing two intercalation peaks to a total of four graphitic peaks (also compare Fig. 3d, 50th cycle), in the CV measurement result in stage 1 intercalated graphite by scan 36, i.e. right before the maximum voltage of 5.1 V is reached (Fig. 8). In both cases the TFSI gallery height is calculated to vary around 7.98 ± .03 Å which is about .1 Å lower than the values obtained in the *ex situ* measurements.

As soon as the de-intercalation starts (scan 54 at around 4.6 V for 20 °C and 49 at 4.9 V for 60 °C, respectively) the XRD spectra undergoes a slight *x*-axis shift to lower 2*θ* values, depicted in the 2nd red line, resulting in a minor increase in periodic repeat distance and gallery height, though remaining the same stage. This process seems to be part of the reason for the first reductive peak in

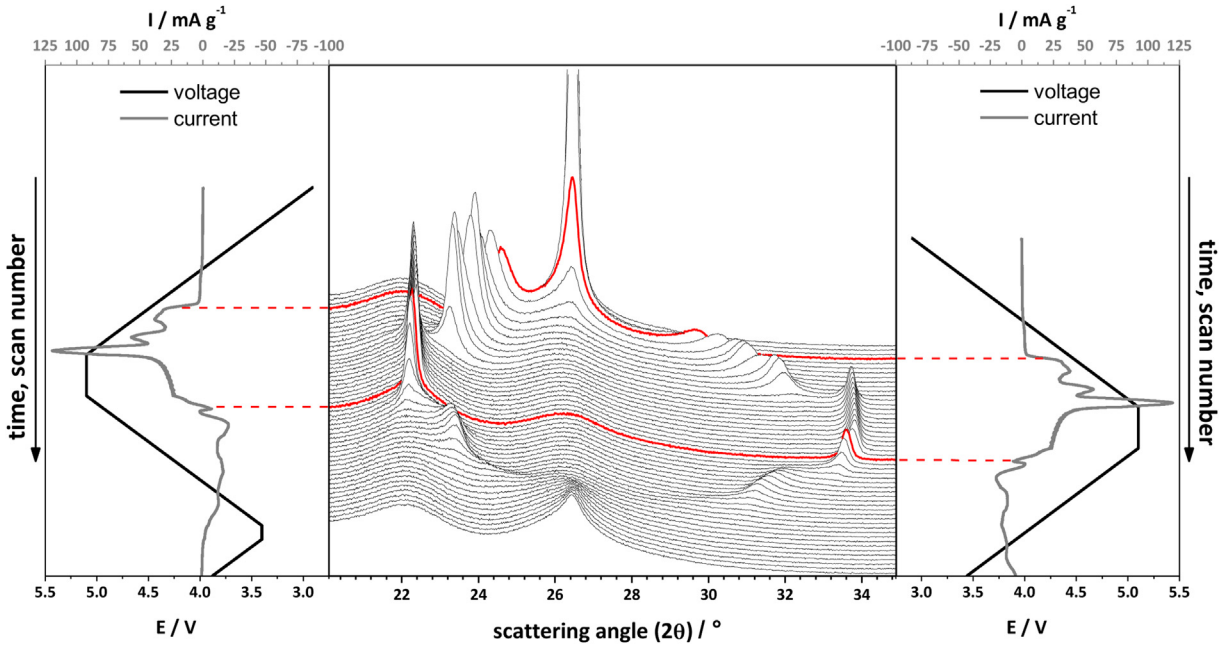

Fig. 8. *In situ* X-ray diffraction patterns as well as cyclic voltammetry profile for the metallic lithium/KS6-graphite dual-ion cell cycled at 60 °C (red lines indicating the beginning of intercalation and deintercalation; scan rate: 50 μV s^{-1}). (For interpretation of the references to colour in this figure legend, the reader is referred to the web version of this article.)

Table 3
The dominant stage index and calculated values for the *in situ* X-ray diffraction measurements of the TFSI intercalation into graphite for the lithium/KS6-graphite dual-ion cell at 20 °C and 60 °C (data corresponding to Figs. 7 and 8).

Temperature/°C	20					60						
Scan number	26[a]	29	45	54[a]	64	27[a]	28	32	36	49[a]	54	60
$d_{(n+2)}/d_{(n+1)}$ ratio	1.20	1.26	1.31	1.31	1.27	1.21	1.24	1.32	1.51	1.51	1.37	1.33
Dominant stage (n)	4	3	2	2	3	4	3	2	1	1	2	2
Periodic repeat distance (I_c)/Å	18.01 ± .06	14.65 ± .02	11.31 ± .13	11.38 ± .11	14.91 ± .07	18.06 ± .03	14.70 ± .06	11.31 ± .10	7.97 ± .01	7.99 ± .01	11.36 ± .10	11.50 ± .03
TFSI gallery height (d_i)/Å	7.96	7.95	7.96	8.03	8.21	8.01	8.00	7.96	7.97	7.99	8.01	8.15
TFSI gallery expansion (Δd)/Å	4.61	4.60	4.61	4.68	4.86	4.66	4.65	4.61	4.62	4.64	4.66	4.80
Cell voltage/V	4.7	4.8	5.2	4.6	4.0	4.6	4.7	4.85	5.1	4.9	4.6	4.2

[a] Corresponding to first intercalation and de-intercalation XRD scans.

Table 4
The experimentally obtained and theoretical specific discharge capacities for different TFSI intercalated graphite stages and compositions (values in bold corresponding to the concluded maximum stoichiometries of the TFSI intercalated graphites at 20 °C and 60 °C).

Experimental			Theoretical			
Temperature/°C	20	60		Stage 1 capacity/mAh g^{-1}	Stage 2 capacity/mAh g^{-1}	Stage 3 capacity/mAh g^{-1}
Upper cut-off voltage/V	5.2	5.1	$(TFSI)C_6$	372	186	124
Discharge capacity (50th cycle)/mAh g^{-1}	**85**	**115**	$(TFSI)C_{12}$	186	98	62
Obtained stage (50th cycle)	1	1	$(TFSI)C_{14}$	160	80	53
			$(TFSI)C_{18}$	124	62	41
			$(TFSI)C_{20}$	**112**	56	37
			$(TFSI)C_{26}$	**86**	43	29

the cyclic voltammetry in both cases. Further de-intercalation leads to a reverse staging transition, namely (2) to (3) for the 20 °C measurement around scan 64 and (1) to (2) for the 60 °C measurement at scan 54. Although the de-intercalation XRD patterns are not as distinct as the intercalation ones, the gallery height broadening to above 8.10 Å during de-intercalation can be observed quite well. Reaching scan 67 (ca. 4.0 V) for the 20 °C measurement and 65 (ca. 4.2 V) for the 60 °C one, respectively, the (002) peak of graphite with a relatively low intensity due to an increasing degree of amorphization reforms. The following cycles, not depicted in this contribution, though showing a similar behavior, indicate that the TFSI gallery height is slowly increasing upon cycling. Taking into account the mentioned *ex situ* results and the kinetic hindrance in the first cycles this seems perfectly reasonable to assume. Moreover, this also explains the deviation in the scattering angle when comparing the *ex situ* and *in situ* results (i.e. Fig. 6, 5.1 V at 20 °C and Fig. 7).

4. Conclusion

Using *ex situ* XRD measurements after constant current cycling as well as *in situ* XRD measurements in combination with cyclic voltammetry for the lithium/KS6-graphite dual-ion cell, with 1 M LiTFSI in $Pyr_{14}TFSI$ electrolyte, TFSI anion intercalation into graphite has been studied. We were able to determine the different phases of TFSI intercalation ("intercalation stages") during and after cycling at varying temperatures and cut-off potentials. We were also able to calculate the periodic repeat distance (I_c), the intercalant guest gallery height (d_i) and the gallery expansion (Δd) for various stages. In addition, considering the TFSI anion dimensions (about 8 Å for the longest axis [47,48]), it is obvious that the TFSI anion cannot be aligned with its long axis perpendicular to the graphene layers. We assume the TFSI anion to be tilted within the layers to an extent that matches the gallery expansion of roughly 4.65 Å. By correlation of the obtained discharge capacities during cycling with the theoretical specific capacities of graphite intercalation (Table 4), we conclude the maximum stoichiometry of the TFSI intercalated graphite to be about $(TFSI)C_{26}$ at 20 °C and $(TFSI)C_{20}$ at 60 °C, respectively. Taking into account simple bond length arguments of the graphite hexagonal sheets and the TFSI anion mentioned above, this proposition seems reasonable. Since we obtained the same stage for the two temperatures though different discharge capacities were observed, applying elevated temperature is able to generate a higher guest concentration in the interlayer gaps compared to the behavior at 20 °C.

Acknowledgments

The authors wish to thank the German Ministry of Education and Research (BMBF) for funding of this work in the project "Insider" (03EK3031A). We gratefully acknowledge the supply of materials by TIMCAL® (KS6 graphite and C-nergy™ Super C65) and Rockwood Lithium® (metallic lithium foil). R. Kloepsch kindly acknowledges "Hans-L.-Merkle Stiftung" for financial support.

References

[1] M. Noel, R. Santhanam, J. Power Sources 72 (1998) 53–65.
[2] J.O. Besenhard, H.P. Fritz, Angew. Chem. Int. Ed. Engl. 22 (1983) 950–975.
[3] M. Winter, J.O. Besenhard, M.E. Spahr, P. Novak, Adv. Mater. 10 (1998) 725–763.
[4] J.O. Besenhard, M. Winter, Pure Appl. Chem. 70 (1998) 603–608.
[5] M. Winter, J.O. Besenhard, Chem. Unserer Zeit 33 (1999) 320–332.
[6] J.O. Besenhard, M. Winter, ChemPhysChem 3 (2002) 155.
[7] D. Billaud, A. Pron, F.L. Vogel, Synth. Met. 2 (1980) 177–184.
[8] N. Bartlett, B. McQuillan, A.S. Robertson, Mater. Res. Bull. 13 (1978) 1259–1264.
[9] A. Jobert, P. Touzain, L. Bonnetain, Carbon 19 (1981) 193–198.
[10] A. Boeck, W. Rüdorff, Z. Anorg. Allg. Chem. 397 (1973) 179–186.
[11] W. Rüdorff, U. Hofmann, Z. Anorg. Allg. Chem. 238 (1938) 1.
[12] W.C. Forsman, F.L. Vogel, D.E. Carl, J. Hoffman, Carbon 16 (1978) 269–271.
[13] E. Bourelle, J. Douglade, A. Metrot, Mol. Cryst. Liq. Cryst. A 244 (1994) 227–232.
[14] X.R. Zhang, N. Sukpirom, M.M. Lerner, Mater. Res. Bull. 34 (1999) 363–372.
[15] M. Winter, Doctoral Thesis, Westfälische Wilhelms-Universität Münster, April 1995, pp. 156–166.

[16] S.E. Millman, G. Kirczenow, D. Solenberger, J. Phys. C: Solid State 15 (1982) 1269–1276.
[17] S.E. Millman, G. Kirczenow, Phys. Rev. B 26 (1982) 2310–2313.
[18] S.A. Safran, D.R. Hamann, Physica B & C 99 (1980) 469–472.
[19] S.A. Safran, Phys. Rev. Lett. 44 (1980) 937–940.
[20] M.S. Dresselhaus, G. Dresselhaus, Adv. Phys. 51 (2002) 1–186.
[21] W. Rüdorff, E. Schulze, Z. Anorg. Allg. Chem. 277 (1954) 156–171.
[22] T. Placke, P. Bieker, S.F. Lux, O. Fromm, H.W. Meyer, S. Passerini, M. Winter, Z. Phys. Chem. 226 (2012) 391–407.
[23] T. Placke, O. Fromm, S.F. Lux, P. Bieker, S. Rothermel, H.W. Meyer, S. Passerini, M. Winter, J. Electrochem. Soc. 159 (2012) 1755–1765.
[24] A. Balducci, W.A. Henderson, M. Mastragostino, S. Passerini, P. Simon, F. Soavi, Electrochim. Acta 50 (2005) 2233–2237.
[25] W.A. Henderson, S. Passerini, Chem. Mater. 16 (2004) 2881–2885.
[26] S.F. Lux, M. Schmuck, G.B. Appetecchi, S. Passerini, M. Winter, A. Balducci, J. Power Sources 192 (2009) 606–611.
[27] A. Brazier, G.B. Appetecchi, S. Passerini, A.S. Vuk, B. Orel, F. Donsanti, F. Decker, Electrochim. Acta 52 (2007) 4792–4797.
[28] G.B. Appetecchi, S. Scaccia, C. Tizzani, F. Alessandrini, S. Passerini, J. Electrochem. Soc. 153 (2006) A1685–A1691.
[29] G.T. Kim, S.S. Jeong, M.Z. Xue, A. Balducci, M. Winter, S. Passerini, F. Alessandrini, G.B. Appetecchi, J. Power Sources 199 (2012) 239–246.
[30] P.C. Howlett, D.R. MacFarlane, A.F. Hollenkamp, Electrochem. Solid State 7 (2004) A97–A101.
[31] J.R. Dahn, J.A. Seel, J. Electrochem. Soc. 147 (2000) 899–901.
[32] J.A. Seel, J.R. Dahn, J. Electrochem. Soc. 147 (2000) 892–898.
[33] T. Ishihara, Y. Yokoyama, F. Kozono, H. Hayashi, J. Power Sources 196 (2011) 6956–6959.
[34] W. Märkle, N. Tran, D. Goers, M.E. Spahr, P. Novak, Carbon 47 (2009) 2727–2732.
[35] T. Placke, P. Bieker, S.F. Lux, O. Fromm, H.W. Meyer, S. Passerini, M. Winter, Z. Phys. Chem. – Themed Issue: Diffusion in Solids (2012).
[36] T.E. Sutto, T.T. Duncan, T.C. Wong, Electrochim. Acta 54 (2009) 5648–5655.
[37] P. Novak, W. Scheifele, M. Winter, O. Haas, J. Power Sources 68 (1997) 267–270.
[38] M. Winter, P. Novak, A. Monnier, J. Electrochem. Soc. 145 (1998) 428–436.
[39] T. Placke, V. Siozios, R. Schmitz, S.F. Lux, P. Bieker, C. Colle, H.W. Meyer, S. Passerini, M. Winter, J. Power Sources 200 (2012) 83–91.
[40] J.P. Olivier, M. Winter, J. Power Sources 97-8 (2001) 151–155.
[41] W. Kohs, H.J. Santner, F. Hofer, H. Schrottner, J. Doninger, I. Barsukov, H. Buqa, J.H. Albering, K.C. Moller, J.O. Besenhard, M. Winter, J. Power Sources 119 (2003) 528–537.
[42] K. Persson, V.A. Sethuraman, L.J. Hardwick, Y. Hinuma, Y.S. Meng, A. van der Ven, V. Srinivasan, R. Kostecki, G. Ceder, J. Phys. Chem. Lett. 1 (2010) 1176–1180.
[43] W.A. Henderson, J.H. Shin, S. Passerini, The Electrochemical Society, Molten Salts XIV: Proceedings of the International Symposion, 2006, p. 444.
[44] B. Ozmen-Monkul, M.M. Lerner, Carbon 48 (2010) 3205–3210.
[45] N. Daumas, A. Herold, C. R. Acad. Sci. C: Chim. 268 (1969) 373.
[46] J.M. Thomas, G.R. Millward, R.F. Schlogl, H.P. Boehm, Mater. Res. Bull. 15 (1980) 671–676.
[47] C. Largeot, C. Portet, J. Chmiola, P.L. Taberna, Y. Gogotsi, P. Simon, J. Am. Chem. Soc. 130 (2008) 2730.
[48] W. Yan, M.M. Lerner, J. Electrochem. Soc. 148 (2001) D83–D87.